HHS Public Access

Author manuscript

Environ Sci Nano. Author manuscript; available in PMC 2019 January 15.

Published in final edited form as:

Environ Sci Nano. 2018 ; 2018(5): 696–707. doi:10.1039/C7EN01046J.

Physicochemical properties of air discharge-generated manganese oxide nanoparticles: Comparison to welding fumes

Larissa V. Stebounova[1], **Natalia I. Gonzalez-Pech**[2], **Thomas M. Peters**[1], and **Vicki H. Grassian**[2,3]

[1]Department of Occupational and Environmental Health, The University of Iowa, Iowa City, IA

[2]Department of Chemistry and Biochemistry, University of California San Diego, La Jolla, CA

[3]Scripps Institution of Oceanography and Department of Nanoengineering, University of California, La Jolla, CA

Abstract

Exposures to high doses of manganese (Mn) via inhalation, dermal contact or direct consumption can cause adverse health effects. Welding fumes are a major source of manganese containing nanoparticles in occupational settings. Understanding the physicochemical properties of manganese-containing nanoparticles can be a first step in understanding their toxic potential following exposure. In particular, here we compare the size, morphology and Mn oxidation states of Mn oxide nanoparticles generated in the laboratory by arc discharge to those from welding collected in heavy vehicle manufacturing. Fresh nanoparticles collected at the exit of the spark discharge generation chamber consisted of individual or small aggregates of primary particles. These nanoparticles were allowed to age in a chamber to form chain-like aggregates of primary particles with morphologies very similar to welding fumes. The primary particles were a mixture of hausmannite (Mn_3O_4), bixbyite (Mn_2O_3) and manganosite (MnO) phases, whereas aged samples revealed a more amorphous structure. Both Mn^{2+} and Mn^{3+}, as in double valence stoichiometry present in Mn_3O_4, and Mn^{3+}, as in Mn_2O_3 and MnOOH, were detected by X-ray photoelectron spectroscopy on the surface of the nanoparticles in the laboratory nanoparticles and welding fumes. Dissolution studies conducted for these two Mn samples (aged and fresh fume) reveal different release kinetics of Mn ions in artificial lysosomal fluid (pH 4.5) and very limited dissolution in Gamble's solution (pH 7.4). Taken together, these data suggest several important considerations for understanding the health effects of welding fumes. First, the method of particle generation affects the crystallinity and phase of the oxide. Second, welding fumes consist of multiple oxidation states whether they are amorphous or crystalline or occur as isolated nanoparticles or agglomerates. Third, although the dissolution behavior depends on conditions used for nanoparticle generation, the dissolution of Mn oxide nanoparticles in the lysosome may promote Mn ions translocation into various organs causing toxic effects.

Correspondence to: Thomas M. Peters; Vicki H. Grassian.

CONFLICTS OF INTEREST

There are no conflicts to declare.

Keywords

Manganese oxide nanoparticles; welding; spark discharge; manganese oxidation states; nanoparticle physicochemical behavior

1. INTRODUCTION

Manganese (Mn) is an abundant metal in the Earth's crust, existing in various oxidation states and phases in the environment.[1] Although a necessary nutrient for humans, Mn exposure in drinking water, food, and dust, near mines or industrial sources, has been associated with adverse health effects, including behavioral changes, lowered intellectual function, impaired motor skills and other adverse neurological effects.[2–5] Inhalation exposure to Mn in occupational settings have been associated with adverse neurological symptoms, such as slower reaction time, hand tremor and Parkinson disease.[6]

Mn spans a range of different stable oxidation states from −3 to +7. Most common oxidation states are +2, +3, +4, +6 and +7 with +2 and +3 oxidation states predominantly found in biological systems.[7, 8] Compounds with Mn in oxidation states +4 and +6 are found in water and near the Earth's surface, whereas species of manganese in the +7 state (permanganates, MnO_4^-) are commonly utilized in the laboratory in oxidation-reduction reactions.[9] Mn^{2+} is believed to be the most abundant form, hence most toxicological studies of transport mechanisms and uptake pathways to the central nervous system (CNS) are based on compounds containing exclusively Mn^{2+}.[2, 10, 11]

Mn^{3+} can enter neuronal cells via the transferrin (Tf) mechanism, the same mechanism known to transport Fe^{3+} into mitochondria for incorporation into iron-containing proteins.[11] The uptake of Mn^{3+} via the Tf mechanism and further translocation into the CNS is slower than the uptake of Mn^{2+}, but it is not negligible and therefore could contribute to Mn toxicity, in addition to other transport mechanisms for Mn into cells.[11] Complexes containing Mn^{3+} can efficiently oxidize and destroy human catecholamines, such as dopamine, which can lead to a neurodegenerative process known as manganism.[12–14] Mn^{2+} does not react with catecholamines, but instead is efficiently oxidized into Mn^{3+} in the presence of O_2^-. The oxidation of dopamine by Mn^{3+} neither produced nor required O_2, and Mn^{3+} was far more efficient than Mn^{2+} and Mn^{4+} in oxidizing the catecholamines. Although Mn^{4+} is a stronger oxidizer than Mn^{3+}, its dopamine oxidizing reaction was diminished greatly after first few minutes due to coating with unreactive Mn^{2+} precipitates.[14]

Welding fumes are a major source of Mn-containing particulate matter (PM) in occupational settings. Depending on the type of welding, welding fumes can contain up to 10% of Mn by mass present mostly as ultrafine and fine PM.[7, 15] Mn as dissolved ions or as ultrafine PM can access the CNS and cause manganism.[12, 13] Studies of occupational exposure to welding fume have reported a number of adverse health effects in welders, such as behavioral changes, fatigue, short-term memory loss and others.[6, 12, 16]

Based on these studies, the Occupational Safety and Health Administration (OSHA) set a limit of 5 mg/m^3 manganese in air averaged over an 8-hour work day.[17] The American

Conference of Governmental Industrial Hygienists (ACGIH) recommended a Threshold Limit Value – Time-Weighted Average (TLV-TWA) of 0.02 mg/m^3 for respirable manganese and its inorganic compounds and 0.1 mg/m^3 for inhalable manganese, which was updated in 2013.[18] However, these occupational exposure limits do not account for potential differences in toxicity as a function of Mn oxidation state and compound. There are only a few attempts to identify the oxidizing forms of Mn in welding emissions.[19] Sequential extraction analysis of welding fume PM collected by respirable samplers indicate that Mn metal in the zero oxidation state along with Mn^{2+} constitute the most abundant fraction followed by Mn^{3+}/Mn^{4+} fraction in the welding fume, typically >50% and ~30–40% of Mn, respectively.[19]

The goal of this study is to characterize physicochemical properties of Mn oxide nanoparticles generated by laboratory methods to investigate the range of oxidation states present at the particle surface and to compare this to welding fume particles collected in the industrial welding environment. One way to produce metal nanoparticles in the laboratory that are similar to welding is through an electric arc discharge created by high voltage applied between two opposing metal rods, which is also known as the spark generation of metal and metal oxide nanoparticles.[20] This method has been used to generate simulated welding fumes[21] and Mn oxide nanoparticles.[13] Mn oxide nanoparticles generated by spark can be characterized by different spectroscopic methods to reveal Mn oxidation states present in nanoparticles produced by air discharge without interference from other metallic elements.

2. MATERIALS AND METHODS

2.1. Spark generation, welding fumes and collection of nanoparticles

Particles were generated by spark discharge system as previously described.[21] Dry, filtered air was delivered to the spark chamber at a flow rate of 5 L/min using a mass flow controller (MFC, MPC20, Porter Instrument, USA). Inside the chamber 5 kV voltage was applied between two identical pure Mn rods (3 mm diameter x 75 mm length, purity 99.5%, Goodfellow Corporation, PA, USA). The aerosol produced in the spark chamber was passed through Po-210 neutralizer and optionally through an agglomeration chamber. Different generation currents between 0.5 and 3 mA were tested for both fresh fume particles and agglomerated particles to establish a correlation between particles size and spark generator current. Bulk samples of fresh fume particles generated at 1 mA and agglomerated particles generated at 2.5 mA were collected at 4 L/min onto 37-mm polyvinyl chloride (PVC) filters (5.0 μm pore size, SKC, Inc., TX, USA) for 48 hours for subsequent analysis by X-ray diffraction and X-ray photoelectron spectroscopy and for dissolution studies.

Welding fume particles generated by robotic and manual metal inert gas (MIG) welding were collected at 12 L/min onto a PVC filter (5.0 μm pore size, SKC, Inc., TX, USA) for 3 hours at a heavy vehicle machining and assembly center.

2.2. Particle size and morphology

The size distributions of the generated particles were measured using a scanning mobility particle sizer (3938, TSI Inc., MN, USA) system consisting of electrostatic classifier (EC,

model 3082), long differential mobility analyzer (DMA, model 3081), nano DMA (model 3085), nano water-based condensation particle counter (CPC, model 3788), and advanced aerosol neutralizer (model 3088). The nano DMA was operated at 1.5 L/min to measure the fresh fume nanoparticles in the size range from 2.1 to 66.1 nm and the long DMA was operated at 0.3 L/min to measure the agglomerated nanoparticles in the size range from 15.1 to 685.4 nm (Figure 1). The stability of generated particle sizes was confirmed by measuring size distributions before and after the collection of nanoparticles on PVC filters. More comprehensive (every 30 min for 12 hours) stability tests for spark generated nanoparticles were conducted in previous studies and it was confirmed that coefficient of variation of the number median diameter remained around 3% for 12 hours.[21]

Nanoparticles generated by spark discharge at 1 mA for fresh fume and at 2.5 mA for agglomerated particles were collected in the aerosol flow onto TEM grids (200-mesh carbon coated Ni grid, 01840N-F, Ted Pella Inc., CA, USA) using nano electrostatic precipitator (ESPnano, model 100, DASH Connector Technology, Inc., WA, USA) for 5 seconds. Primary particle diameter, nanoparticle morphology and agglomeration state were evaluated from TEM images acquired using high resolution transmission electron microscope (HRTEM, JEOL-2100F, JEOL Ltd., Japan) and analyzed by ImageJ software (version 1.50i, NIH, USA).

2.3. Mn nanoparticles crystallinity and oxidation states

Diffraction patterns of the two bulk samples were measured using X-Ray Diffractometer (XRD, D8 Advance, Bruker AXS Inc., WI, USA) with CuKα radiation (λ = 1.5406 Å) in the range $10^{\circ} \leq 2\theta \leq 90^{\circ}$ operated at 40 kV and 40 mA. The sample holder was modified by inserting a Si crystal zero diffraction plate designed for small samples (24.6 mm diameter x 1 mm thickness, MTI Corporation, CA, USA) into Bruker's original sample holder. XRD patterns of spark generated Mn samples were analyzed in DIFFRAC.EVA software suite (Bruker AXS Inc., WI, USA) and the peaks were matched with reference patterns of different Mn oxides available from Joint Committee on Powder Diffraction Standards (JCPDS) cards: MnO (JCPDS 07–0230), Mn_2O_3 (JCPDS 24–0508) and Mn_3O_4 (JCPDS 80–03820).

A custom-designed Kratos Axis Ultra X-ray photoelectron spectroscopy (XPS) system previously described[22] was used to collect core photoelectron spectra of Mn nanoparticles generated by spark discharge system and welding fume particles collected at the industrial site. The nanoparticles were removed from the PVC filters and pressed directly into a carbon tape attached to XPS sample holder for the analysis. All spectra were calibrated using the adventitious carbon 1s peak at 285.0 eV. A Shirley-type background was subtracted from each spectrum to account for inelastically scattered electrons that contribute to the broad background. CasaXPS software (Version 2.3.17PR1.1, Casa Software Ltd, UK) was used to process the XPS data. Transmission corrected relative sensitivity factor (RSF) values from the Kratos library were used for elemental quantification, as implemented into CasaXPS.

2.4. Dissolution studies of Mn oxide nanoparticles in simulated biological fluids

Dissolution of Mn oxide nanoparticles was measured in four simulated fluids: artificial lysosomal fluid (ALF) (pH=4.5); Gamble's solution (pH=7.4); acidic solution (pH=4.5); and phosphate buffer (pH=7.4). pH in the acidic solution and the phosphate buffer (10mM Na_2HPO_4) was adjusted by adding HCl. ALF and Gamble's solutions were prepared as previously described using milliQ water.[23] The solutions were added to the nanoparticles (40 μg/ml) and then incubated for 24 hours at room temperature under continuous mixing. Aliquots of 1 ml were taken at different times for analysis. The solutions were filtered with 0.2 μm polyethersulfone syringe filters (Puradisc 25AS, Whatman) to remove solid particles and analyzed with an inductively coupled plasma - mass spectrometer (ICP-MS) (iCAP RQ ICP-MS, Thermo Fisher Scientific, MA, USA). A 100 ppm Mn standard for ICP-MS (Inorganic Ventures, Christiansburg, VA) was diluted with 2% HNO_3 (Trace Metal Grade, Fisher Scientific LLC, Pittsburgh, PA) to concentrations of 0.5, 1, 2, 5, 10, 20, 50, 100, 200 and 500 μg/L to measure the calibration curve. Yttrium was added to all samples as an internal standard (ICP-MS Internal Standard solution, Inorganic Ventures, Christiansburg, VA, USA). ICP-MS samples were acidified using HNO_3. Dissolution experiments were conducted in triplicates.

Samples were also analyzed for changes in size distributions of Mn nanoparticles using dynamic light scattering (DLS) (Beckman-Coulter Delsa Nano C, FL, USA) during dissolution experiments. As soon as the particles were exposed to the corresponding solution, they were sonicated (amplitude of 40% in 20 s on and 10 s off intervals, Sonics Vibra-cell, Newtown, CT, USA) for two minutes to create an even suspension. Aliquots of 3 ml were taken at the same times as for ICP-MS analysis, for DLS analysis, and the samples were returned to the original 50 ml tubes to continue mechanical mixing after the DLS analysis.

3. RESULTS AND DISCUSSION

3.1. Particle size distributions and morphology

The particle size distributions of the fresh fume particles shifted to larger diameters with increased discharge current applied to the Mn rods (Figure 2A). The number mean diameter of fresh fume Mn nanoparticles increased from 25 ± 2 nm to 41 ± 0.2 nm when the current was increased from 0.5 mA to 2 mA (Table 1). The total number concentration also increased with increasing current (Table 1). These results are consistent with observations of Park et al. for welding rod electrodes.[21] High-resolution TEM imaging of the fresh fume nanoparticles reveals that larger Mn nanoparticles consist of clusters of the primary particles, as can be seen in Figure 3A. The diameter of individual primary particles is approximately 5 nm, as shown in the inset of Figure 3A and as measured from TEM images in ImageJ software (Figure 3C). Spark generation current of 1 mA was used to collect fresh fume Mn nanoparticles for further bulk analyses.

Size distributions of Mn nanoparticles generated by spark and after passing through the coagulation chamber are shown in Figure 2B. The size distribution measured at 1 mA was bimodal with a particle mean diameter of 163 nm. As the current increased, we observed an

increase in total number concentration and a shift of number mean diameter to smaller size, while the distributions became more log-normal (Table 1 and Figure 2B). The particles formed chain-like aggregates/agglomerates as can be seen from the TEM image in Figure 3B. The TEM image clearly shows that the aggregates are formed from primary particles with a diameter of ~ 5 nm. These results indicate that a longer agglomeration time (e.g. in the agglomeration chamber) leads to larger agglomerates of the same primary particles and higher generation currents produce larger total number of particles.

A representative TEM image of a sample collected in a heavy vehicle machining and assembly center near manual welding is shown in Figure 3D. The morphology is very similar to the spark generated agglomerated Mn nanoparticles, but the diameters of primary particles differ. As can be seen in Figure 3D, primary particle diameters vary from 5 nm to 10–20 nm. This difference may be due to different chemical composition of welding fume particles. This observation also agrees with the welding fume morphology reported by others for lab-generated and industrial welding fume particles.[21, 24] Furthermore, particles generated in real-world environments, such as welding at a heavy vehicle machining and assembly plant, have very high concentrations near the generation source leading to very fast agglomeration of nanoparticles before they are exposed to the surrounding atmosphere.

3.2. Chemical composition and Mn oxidation states of spark-generated Mn nanoparticles and welding fumes

X-ray diffraction patterns of Mn bulk samples are shown in Figure 4. The XRD pattern of fresh fume nanoparticles reveals some crystalline structure, while the XRD pattern of agglomerated nanoparticles shows mostly an amorphous structure (Figure 4). Agglomerated nanoparticles were produced with a higher generation current of 2.5 mA compared to fresh fume generation current of 1 mA. It was shown before that higher generation currents produce higher concentrations of NO_x and O_3,[21] which in turn can react with Mn resulting in embedded amorphous compounds. Also, similar phenomenon was observed by Guo et al. for carbon-filled manganese oxide–carbon nanocomposite particles.[25] In that study, MnO_x agglomerates embedded with carbon were amorphous, while pure MnO_x nanoparticles showed Mn_3O_4 and Mn_2O_3 crystalline phases.

The phases observed in the XRD pattern of fresh fume were matched with diffraction lines of reference materials such as hausmannite (Mn_3O_4), bixbyite (Mn_2O_3) and manganosite (MnO) (Figure 4).[26] XRD reveals that hausmannite and bixbyite are the dominant phases in the fresh fume sample while MnO is present in smaller quantity in the fresh fume Mn nanoparticles (Figure 4). Mn_3O_4 has spinel structure with Mn^{2+} in tetragonal and Mn^{3+} in octahedral coordination.[27] Both Mn_3O_4 and MnO have cubic crystal lattice structures.

Fresh fume, agglomerated Mn and industrial welding fume samples were also analyzed by X-ray photoelectron spectroscopy. Peaks corresponding to Mn(2p), O(1s), C(1s), N(1s) and F(1s) were detected in survey spectra of spark-generated samples, while survey spectrum of welding fume sample has peaks corresponding to Fe(2p), Mn(2p), O(1s), C(1s) and Cl(2p) (Suppl. Figure 1). Mn(2p), O(1s), C(1s) and N(1s) regions were analyzed with high resolution XPS and fit with several different components as shown in Figure 5A for the fresh fume sample and in Figure 5B for the agglomerated Mn nanoparticles. In the XPS spectra of

both samples, Mn(2p) transition has a doublet with peaks at 642.5 eV($2p_{3/2}$) and 654 eV($2p_{1/2}$) due to spin-orbit splitting with the peak area ratio of 2:1 (Suppl. Figure 1). Therefore, only Mn ($2p_{3/2}$) peak is fitted with components. The positions, FWHM and percent concentrations of the XPS fitted components are shown in Table 2.

Overall, the Mn $2p_{3/2}$ peaks in fresh fume and agglomerated samples are fit with seven components (Figures 5A, B). The shape and heights of the fitted components for fresh fume sample are similar to XPS fit components of a manganite (MnOOH) standard reported by Ilton et al.[28] or Mn_2O_3 ($2p_{3/2}$) spectrum as the two compounds have very similar XPS fits.[28, 29] The peak positions of Mn (2p) components (Table 2) are slightly shifted possibly due to an overlapping of binding energies for Mn oxide and Mn oxyhydroxide present in Mn fresh fume sample. In addition, different Gaussian to Lorentzian ratios were used in this study (30 *vs.* 50 in Ref. 28), so the peaks are slightly wider and can have slightly shifted fitting maxima.

The component at 641.4 eV has the highest percent concentration in the fresh fume sample (Table 2). This peak is representative of Mn^{3+} oxidation state which can be found in bixbyite (Mn_2O_3), manganite (MnOOH) or in hausmannite (Mn_3O_4).[28, 30] The second and third largest components at 642.4 eV and 643.3 eV have also been identified as Mn^{3+} in the manganite and hausmannite spectra.[28–30] A small peak at 640.1 eV fits the tail at lower binding energies and could be attributed to the presence of Mn^{2+},[29, 30] which we observe in XRD patterns for fresh fume Mn nanoparticles. For the agglomerated sample, the peak at 640.5 eV constitutes 11.5% of Mn(2p) peak area and is assigned to Mn^{2+} (Figure 5B).[29, 30] The peak positions and relative intensities of the Mn(2p) peak components in the agglomerated sample (Figure 5B) do not resemble XPS spectra of MnO but resemble more closely those found for haumannite.[28–30]

Peaks around 644 eV, 645 eV and 647 eV fit the tails of the spectra for both samples due to shake up and inelastic scattering.[29] The lack of strong peak below 641 eV in the fresh fume Mn(2p) spectrum leads to a conclusion that the fresh fume Mn nanoparticles surface is composed of Mn atoms in the +3 oxidation state as in manganite (MnOOH) or in bixbyite (Mn_2O_3), while stronger Mn^{2+} component in the agglomerated Mn nanoparticles indicates the presence of hausminnite (Mn_3O_4) on the sample's surface.

In the O(1s) region, the O(1s) peak for fresh fume sample (Figure 5A) can be fit to three components: 530.3 eV due to O^{2-}; 531.5 eV due to OH^- and/or CO_3^{2-}; and 533.9 eV due to adsorbed H_2O.[30] Idealized manganite composition requires equal abundance of O^{2-} and OH^- groups. We observe an oxide to hydroxide ratio of 2.3 in fresh fume Mn sample (Table 2), suggesting that Mn_2O_3 as well as MnOOH are present on the surface of the fresh fumed sample. The O(1s) region from the agglomerated sample (Figure 5B) is more complex and has an extra component at 529.5 eV in addition to the three components found in fresh fume O(1s) region, which corresponds to chemisorbed O on the defect sites of Mn oxides similar to O chemisorbed on Cu oxide surface.[31]

The C(1s) peak is fit with three components for both fresh fume and agglomerated samples (Figures 5A, B). Components at 285 eV, 286 eV and 289 eV are due to hydrocarbons,

alcohols and ethers, and ketones, correspondingly, and are typical for the adventitious carbon. N(1s) peak at 407 eV indicates that nitrates are present on the fresh fume and agglomerated samples' surfaces.[32] The presence of nitrates on the nanoparticle surfaces can increase their dissolution rate in the aqueous environments and therefore make Mn more bioavailable.[33] In addition, multiple components in O(1s) and C(1s) spectrum regions confirm the presence of several carbonaceous species and hydrates on the agglomerated sample surface, which are probably trapped in the void areas of the chain-like agglomerates of Mn nanoparticles. These features can also change the dissolution rate of these nanoparticles.

XPS spectrum of welding fume collected at the heavy vehicle machinery and assembly site was also analyzed and compared to the XPS spectra of Mn fresh fume and agglomerated nanoparticles. Fe(2p), Mn(2p), O(1s) and C(1s) and N(1s) regions were analyzed with high resolution XPS. Fitted components of first four regions are shown in Figure 5C. The N(1s) region does not have a strong component corresponding to nitrates and is shown in Supplementary materials (Suppl. Figure 2). Mn(2p) peak was fitted with 7 components. The peak shape, positions of components and their relative atomic concentrations (Table 2) indicate a presence of at least two oxidation states of Mn^{2+} and Mn^{3+}.[28] The peak at 640.0 eV indicates a presence +2 oxidation state. Spark generated agglomerated Mn nanoparticles had 11.5% of Mn in +2 oxidation state, while industrial welding sample has 19.5% of Mn in +2 oxidation state. The fitted components at 641.1 eV, 641.9 eV and 642.9 eV are in agreement with the convolution of the components from Mn^{2+} and Mn^{3+} oxidation states.[28] The Mn components of welding fume sample more closely resemble Mn components of the agglomerated Mn nanoparticles. A presence of Mn^{4+} is unlikely in any of the samples analyzed in this work which would be indicated by a strong component at 642 eV.[28]

The Fe(2p) peak observed in industrial welding fume sample was fit with 6 components. Fitting parameters of goethite standard (α-FeOOH) from Ref. 34 were used to fit Fe(2p) peak (Table 2). Components at 710.1 eV, 711.1 eV, 712.1 eV and 713.2 eV are in close agreements with the peaks predicted theoretically and detected in standard samples of α-FeOOH. The low binding energy component at 709.1 eV (pre-peak) has been observed in XPS spectra of iron oxides and hydroxides and could appear due to Fe ions with a lower than normal oxidation state produced by defects in the neighboring sites.[34] A peak at 713.9 eV is identified as a surface peak by Grosvenor et al. and could appear due to differences between bulk and surface structures in the material.

O(1s) components of welding fume sample at 530.1 eV, 531.3 eV and 532.7 eV are from O^{2-}, OH^{-} and an adsorbed H_2O, correspondingly (Figures 5C). Hydroxides at 531.3 eV constitute 31% in welding fume sample (Table 2). This observation indicates the presence of oxyhydroxides of Mn and Fe. Both Mn and Fe oxyhydroxides require equal abundance of O^{2-} and OH^{-} groups. Extra O^{2-} groups observed in O(1s) spectrum most likely contribute to Mn oxides present in the sample. C(1s) spectrum in Figure 5C has the characteristic shape and components of adventitious carbon with 61% of hydrocarbons, 34% of esters and alcohols and 5% of ketons (Table 2).

A comparison of these XPS spectra show that Mn nanoparticles generated by spark discharge in the laboratory have different physicochemical properties depending on their agglomeration state. Fresh fume particles, which consist of single or a few of primary Mn nanoparticles, have two dominant Mn crystal phases as detected by XRD. The first phase Mn_3O_4, known as hausmannite, has Mn in two valence states, Mn^{2+} and Mn^{3+}, and the second major phase has Mn^{3+} in Mn_2O_3. The surface analysis of fresh fume Mn nanoparticles by XPS revealed mostly Mn^{3+} oxidation state. Agglomerated Mn nanoparticles produced by spark discharge consist of the same primary Mn nanoparticles, which form chain agglomerates up to a few of microns in size. Agglomerated nanoparticles appear amorphous in XRD, but still consist of primary nanoparticles and may retain their Mn^{2+}/Mn^{3+} oxidation states. The XPS analysis of the agglomerated sample reveal that Mn^{2+} is present on the sample surface along with the Mn^{3+}.

The morphology of agglomerated sample closely resembles morphology of welding fume sample collected at an industrial site. The welding fume particles consist of mostly Fe and Mn oxyhydroxides with a ratio of 85%Fe:15%Mn. While oxidation state of Fe in welding fume sample is clearly identified as Fe^{3+} and matched with α-FeOOH, XPS analysis of Mn peak from welding fume is more complicated due to convolution of multiplex components from two oxidation states, Mn^{2+} and Mn^{3+}. The Mn(2p) peak in welding fume XPS has more similarities with Mn(2p) peak measured in the agglomerated Mn sample. The similar morphology and surface properties of spark generated agglomerated Mn nanoparticles and industrial welding fume sample allows the use of Mn nanoparticles generated in the lab as proxies to study bioavailability and toxicity properties of these nanoparticles and then relate these data to the bioavailability and toxicity of Mn found in welding fumes generated in industrial environments as discussed below.

3.3. Dissolution and size changes of Mn oxide nanoparticles in simulated lung fluids

Because of the interest in the health effects of these nanoparticles, dissolution studies were performed in simulated lung fluids. These dissolution studies can provide guidance toward understanding the availability of transition metal ions that may exhibit toxic behavior.[35] Due to limited amount of the industrial welding fume sample, dissolution studies were not carried out with the field collected particles. As the similarity was previously stated, insights of their bioavailability can be drawn from the behavior of the spark-generated agglomerated Mn nanoparticles. Fresh fume Mn nanoparticles were also studied for comparison. Their dissolution behavior in different simulated lung fluids is summarized in Figure 6. As expected, both samples are stable at circumneutral pH (phosphate buffer and Gamble's solutions). Most interesting is that low pH by itself seems to have no effect in their solubility; the dissolution happens only in the ALF solution, presumably due to the presence of a large amount of citrate which is added to ALF to represent or mimic ligand-coordinating organic content of biological fluids (e.g. proteins). The ligand-promoted dissolution effect of citric acid has also been observed in circumneutral pH for other metal oxide nanoparticles.[36] The increased solubility of metal-contained particulates in ALF versus other biological fluids (Gamble's and buffer solution) has also been reported.[37]

A significant difference is observed in the kinetics of dissolution in ALF buffer between fresh fume (Figure 6A) and agglomerated nanoparticles (Figure 6B). Fresh fume nanoparticles dissolve quickly during the first two hours and reach a steady state after that. Agglomerated nanoparticles keep dissolving after 24 hours. To corroborate that dissolution reaches a steady state for fresh fume nanoparticles, an extra experiment was conducted until the full dissolution was reached, at ~48 hours. This could be due to the presence of hydroxides and nitrates on the fresh fume sample surface,[33] but also the degree of agglomeration plays a factor as potentially less surface area is available for the ligand-promoted dissolution process. To verify the effect of the surface impurities, a similar dissolution study was conducted with a single phase Mn oxide (Mn_3O_4) nanocrystal (Suppl. Figure 3D). The characterization of the reference sample (SEM, TEM and XRD) is also shown in Suppl. Figure 3. Most interestingly is that the dissolution of the Mn_3O_4 nanocrystals was not significant in any of the analyzed conditions, which indicates these nanocrystals are not good proxies for investigating spark generated and welding particles, potentially due to a lack of surface defects in the crystalline materials or other differences that play a role in dissolution of the spark generated nanoparticles.

Characterization of particle sizes by DLS during the dissolution studies were carried out to verify the effect of agglomeration. Figure 7 summarizes the changes in particle sizes with time in different solutions for fresh fume. A similar analysis was carried out for agglomerated nanoparticles, correspondingly; however, because of large agglomerate sizes (~10 μm), clear conclusions cannot be drawn from this experiment. Similar to TEM analysis in Figure 3, DLS analysis also showed smaller than 500 nm particle sizes for fresh fume nanoparticles (Figure 7) at the start of dissolution experiments (0 h). The middle and top graphs show changes in peak positions and relative intensities after 1 hour and 24 hours, correspondingly. As can be seen in Figure 7A, fresh fume nanoparticles have agglomerates around 200 nm, which completely disappear after 24 hours in the acidic solution (pH=4.5), even when dissolution is not significant (Figure 6A). On the other hand, fresh fume nanoparticles incubated in the buffer with pH 7.4 (Figure 7B) show no significant change in size distribution. Fresh fume nanoparticles incubated in Gamble's solution form large aggregates (around 4μm) that are stable in the solution after 24 hours (Figure 7C). Particle aggregation in solutions with high ionic strength has been reported for other metal oxides and is usually accompanied by sedimentation.[38, 39] The stability of these aggregates can be explained by the organic ligands found in the Gamble's solution (sodium acetate and citrate), which can act as coordinating surface ligands that stabilize the nanoparticles. As expected, when fresh fume Mn nanoparticles are exposed to ALF solution, the particle size decreases in the first hour; and no particles are detected by the DLS after 24 hours due to dissolution (Figure 7D).

4. CONCLUSIONS

This study shows that spark generated nanoparticles have different physicochemical properties depending on whether the particles were allowed to agglomerate or collected fresh near the generation site. Several crystal lattice structures were found in fresh fume Mn nanoparticles by the XRD, including Mn_3O_4, Mn_2O_3 and MnO, while mostly Mn^{3+} was detected on fresh fume sample surface by the XPS. XPS analysis indicates that

oxyhydroxides along with some nitrates are present in fresh fume Mn. XRD analysis revealed amorphous structure of agglomerated Mn nanoparticles, while XPS showed Mn^{2+} and Mn^{3+} present in the sample most likely as a double valence oxide, Mn_3O_4. The lack of signal in the XRD of the agglomerated sample could be due to embedded impurities produced by higher generation currents. Mn oxidation states found in the agglomerated sample are similar to those found in the industrial welding fume sample. Welding fume particulates usually form chain-like agglomerates and as such show similarities with the agglomerates Mn nanoparticles generated in the lab. Using these lab-generated nanoparticles, dissolution study showed that 60% of fresh fume and agglomerated nanoparticles dissolved in the first 24 hours in artificial lysosomal fluid with almost no dissolution in all other buffers tested in this work. The dissolution kinetics were different between two samples, where fresh fume sample dissolved faster in the first two hours while agglomerated nanoparticles showed more steady dissolution during 24 hours in ALF buffer. The presence of nitrates and hydroxides on the fresh fume sample surface could account for its faster dissolution, while the agglomerated nanoparticles were de-agglomerating and dissolving the impurities in the first few hours in ALF solution. The structural similarities between welding fume sample and the agglomerated Mn nanoparticles could indicate that welding fume particles will have similar Mn^{3+} and Mn^{2+} ion release rate within the lung where inhaled nanoparticles come into contact with alveolar and interstitial macrophages. Overall, this study shows for the first time a comparison of the behavior of laboratory spark generated manganese oxide nanoparticles, welding fume nanoparticles and a crystalline manganese oxide material. The crystalline material behaves very differently than the other samples and would therefore be a poor model for simulating the physical chemical properties of welding fumes, whereas the spark-discharge samples are in fact proposed to be good model systems.

Supplementary Material

Refer to Web version on PubMed Central for supplementary material.

ACKNOWLEDGEMENTS

The authors would like to acknowledge use of the University of Iowa Central Microscopy Research Facility, a core resource supported by the Vice President for Research & Economic Development, the Holden Comprehensive Cancer Center and the Carver College of Medicine. Financial support for this work was provided by National Institute for Occupational Safety and Health grant number R01 OH010238.

REFERENCES

1. Post JE, Proceedings of the National Academy of Sciences of the United States of America, 1999, 96, 3447–3454. [PubMed: 10097056]
2. Peres TV, Schettinger MRC, Chen P, Carvalho F, Avila DS, Bowman AB and Aschner M, BMC Pharmacol. Toxicol, 2016, 17, 20. [PubMed: 27132129]
3. Vincent JH, Journal of Environmental Monitoring, 2012, 14, 340–347. [PubMed: 22109739]
4. Bowler RM, Kornblith ES, Gocheva VV, Colledge MA, Bollweg G, Kim Y, Beseler CL, Wright CW, Adams SW and Lobdell DT, Neurotoxicology, 2015, 49, 139–148. [PubMed: 26096496]
5. Oulhote Y, Mergler D, Barbeau B, Bellinger DC, Bouffard T, Brodeur ME, Saint-Amour D, Legrand M, Sauve S and Bouchard MF, Environmental Health Perspectives, 2014, 122, 1343–1350. [PubMed: 25260096]

6. Harris RC, Lundin JI, Criswell SR, Hobson A, Swisher LM, Evanoff BA, Checkoway H and Racette BA, Parkinsonism & Related Disorders, 2011, 17, 672–676. [PubMed: 21724446]
7. Taube F, Ann. Occup. Hyg, 2013, 57, 6–25. [PubMed: 22997412]
8. Michalke B, Halbach S and Nischwitz V, Journal of Environmental Monitoring, 2007, 9, 650–656. [PubMed: 17607384]
9. Hem JD, International Association of Scientific Hydrology, 1963, Bulletin, 8:3, 30–37.
10. Karmakar A, Zhang QL and Zhang YB, Journal of Food and Drug Analysis, 2014, 22, 147–160. [PubMed: 24673911]
11. Gunter TE, Gerstner B, Gunter KK, Malecki J, Gelein R, Valentine WM, Aschner M and Yule DI, Neurotoxicology, 2013, 34, 118–127. [PubMed: 23146871]
12. Bowler RM, Gysens S, Diamond E, Nakagawa S, Drezgic M and Roels HA, Neurotoxicology, 2006, 27, 315–326. [PubMed: 16343629]
13. Elder A, Gelein R, Silva V, Feikert T, Opanashuk L, Carter J, Potter R, Maynard A, Finkelstein J and Oberdorster G, Environmental Health Perspectives, 2006, 114, 1172–1178. [PubMed: 16882521]
14. Archibald FS and Tyree C, Arch. Biochem. Biophys, 1987, 256, 638–650. [PubMed: 3039917]
15. Zimmer AT, Baron PA and Biswas P, J. Aerosol. Sci, 2002, 33, 519–531.
16. Antonini JM, Critical Reviews in Toxicology, 2003, 33, 61–103. [PubMed: 12585507]
17. OSHA, Air contaminants, Occupational Safety and Health Administration., http://www.osha.gov/comp-links.html, 2007.
18. ACGIH, Manganese, elemental and inorganic compounds, American Conference of Governmental Industrial Hygienists 2012.
19. Hanley KW, Andrews R, Bertke S and Ashley K, Journal of Occupational and Environmental Hygiene, 2015, 12, 774–784. [PubMed: 26011602]
20. Byeon JH, Park JH and Hwang JH, J. Aerosol. Sci, 2008, 39, 888–896.
21. Park JH, Mudunkotuwa IA, Kim JS, Stanam A, Thorne PS, Grassian VH and Peters TM, Aerosol Science and Technology, 2014, 48, 768–776.
22. Baltrusaitis J, Usher CR and Grassian VH, Phys. Chem. Chem. Phys, 2007, 9, 3011–3024. [PubMed: 17551626]
23. Marques MRC, Loebenberg R and Almukainzi M, Dissolution Technologies, 2011, 18, 15–28.
24. Stephenson D, Seshadri G and Veranth JM, AIAH Journal, 2003, 64, 516–521.
25. Guo JC, Liu Q, Wang CS and Zachariah MR, Advanced Functional Materials, 2012, 22, 803–811.
26. Jankovsky O, Sedmidubsky D, Simek P, Sofer Z, Ulbrich P and Bartunek V, Ceramics International, 2015, 41, 595–601.
27. Huang HW, Yu Q, Peng XS and Ye ZZ, Chemical Communications, 2011, 47, 12831–12833. [PubMed: 22044879]
28. Ilton ES, Post JE, Heaney PJ, Ling FT and Kerisit SN, Appl. Surf. Sci, 2016, 366, 475–485.
29. Biesinger MC, Payne BP, Grosvenor AP, Lau LWM, Gerson AR and Smart RS, Appl. Surf. Sci, 2011, 257, 2717–2730.
30. Nesbitt HW and Banerjee D, American Mineralogist, 1998, 83, 305–315.
31. Eren B, Heine C, Bluhm H, Somorjai GA and Salmeron M, Journal of the American Chemical Society, 2015, 137, 11186–11190. [PubMed: 26275662]
32. Baltrusaitis J, Jayaweera PM and Grassian VH, Phys. Chem. Chem. Phys, 2009, 11, 8295–8305. [PubMed: 19756286]
33. Batrusaitis J, Chen HH, Rubasinghege G and Grassian VH, Environmental Science & Technology, 2012, 46, 12806–12813. [PubMed: 23057678]
34. Grosvenor AP, Kobe BA, Biesinger MC and McIntyre NS, Surface and Interface Analysis, 2004, 36, 1564–1574.
35. Pettibone JM, Adamcakova-Dodd A, Thorne PS, O'Shaughnessy PT, Weydert JA and Grassian VH, Nanotoxicology, 2008, 2, 189–204.
36. Mudunkotuwa IA, Rupasinghe T, Wu C-M and Grassian VH, Langmuir, 2012, 28, 396–403. [PubMed: 22122742]

37. Hedberg Y, Hedberg J, Liu Y and Wallinder IO, Biometals, 2011, 24, 1099–1114. [PubMed: 21691833]

38. Vikesland PJ, Rebodos RL, Bottero JY, Rose J and Masion A, Environmental Science-Nano, 2016, 3, 567–577.

39. French RA, Jacobson AR, Kim B, Isley SL, Penn RL and Baveye PC, Environmental Science & Technology, 2009, 43, 1354–1359. [PubMed: 19350903]

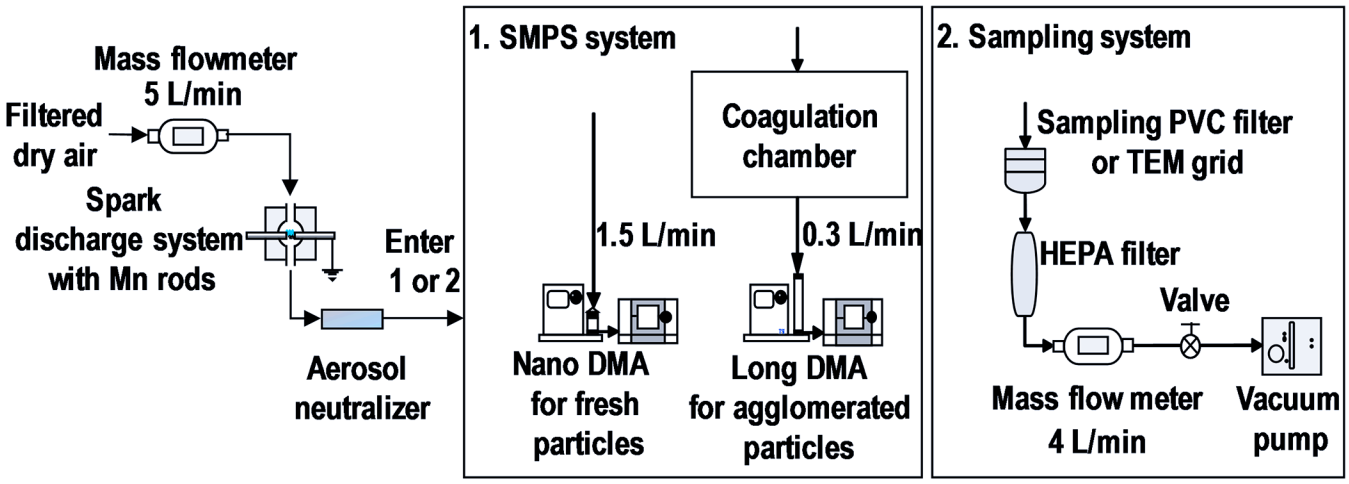

Figure 1.
Mn nanoparticle generation, sizing and sampling systems.

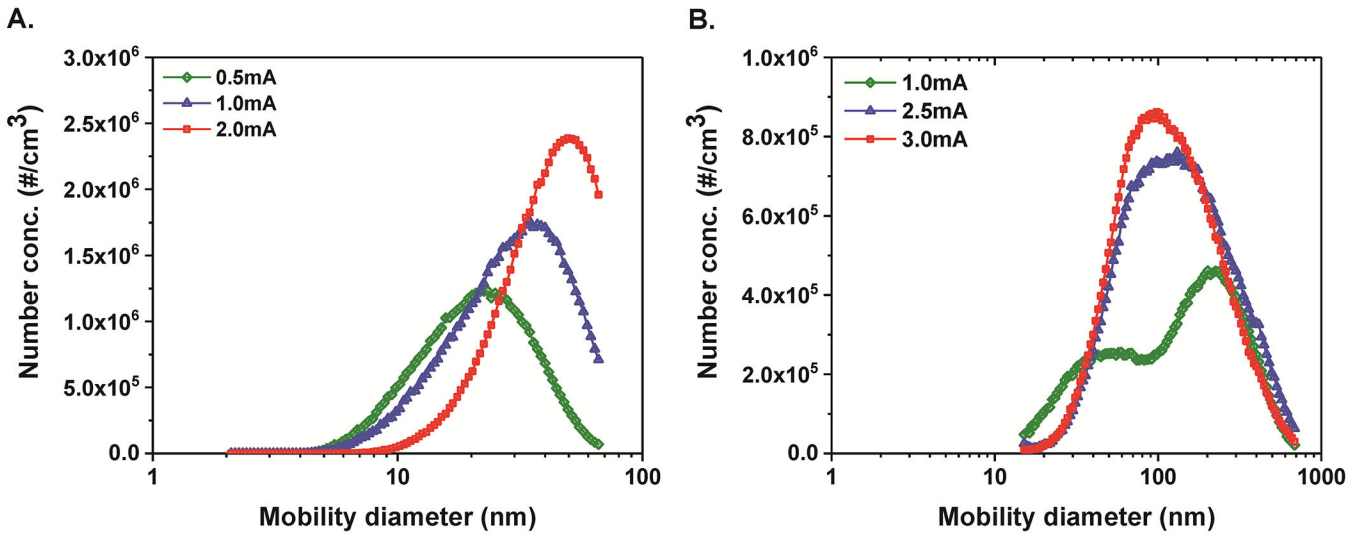

Figure 2.

Size distributions of fresh fume (A) and agglomerated (B) Mn nanoparticles generated by spark discharge at different currents as measured by the SMPS.

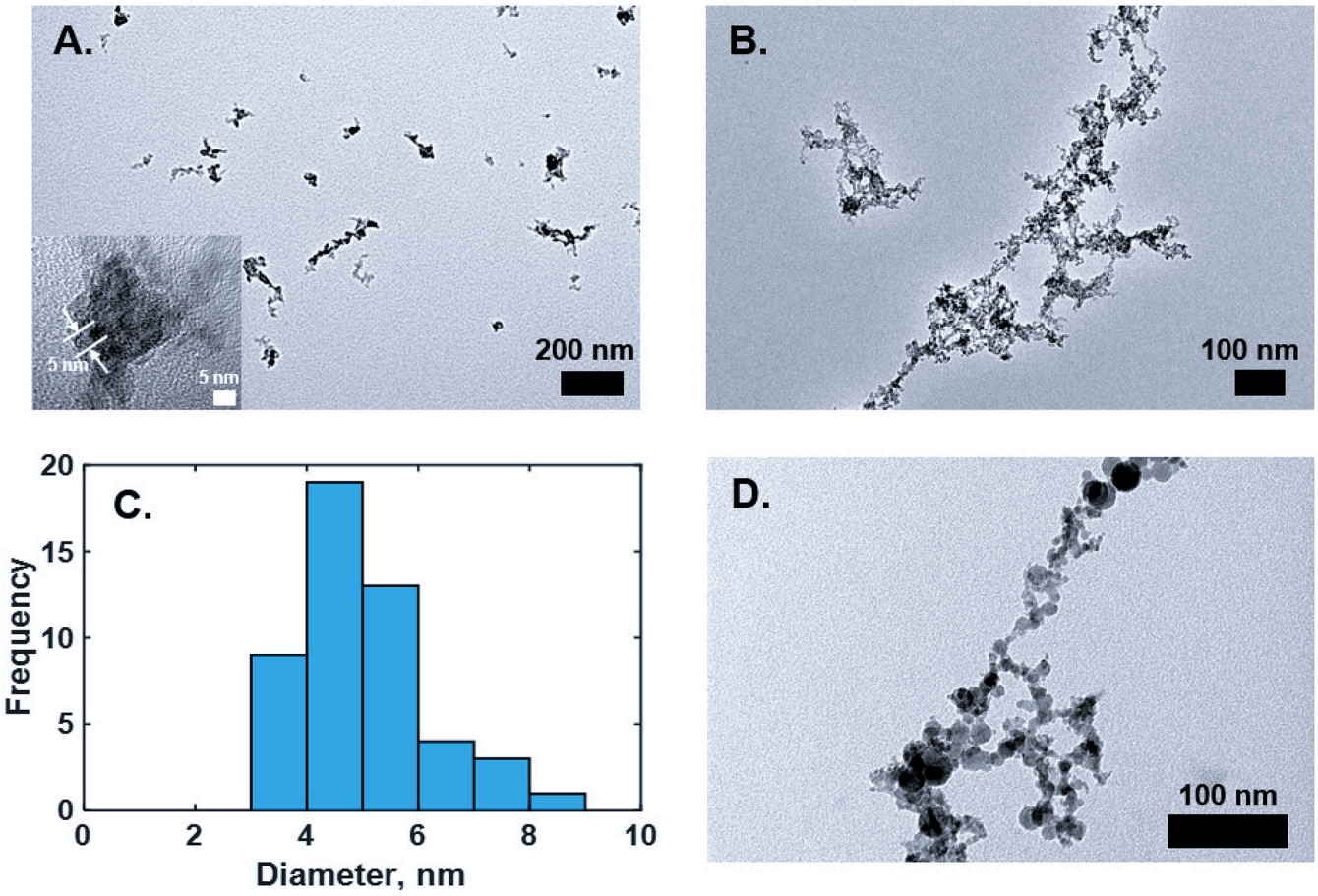

Figure 3.

High-resolution TEM images of fresh fume (A) and agglomerated (B) Mn nanoparticles. (C) A histogram of primary particle diameters measured from the TEM images. (D) High-resolution TEM image of industrial welding sample.

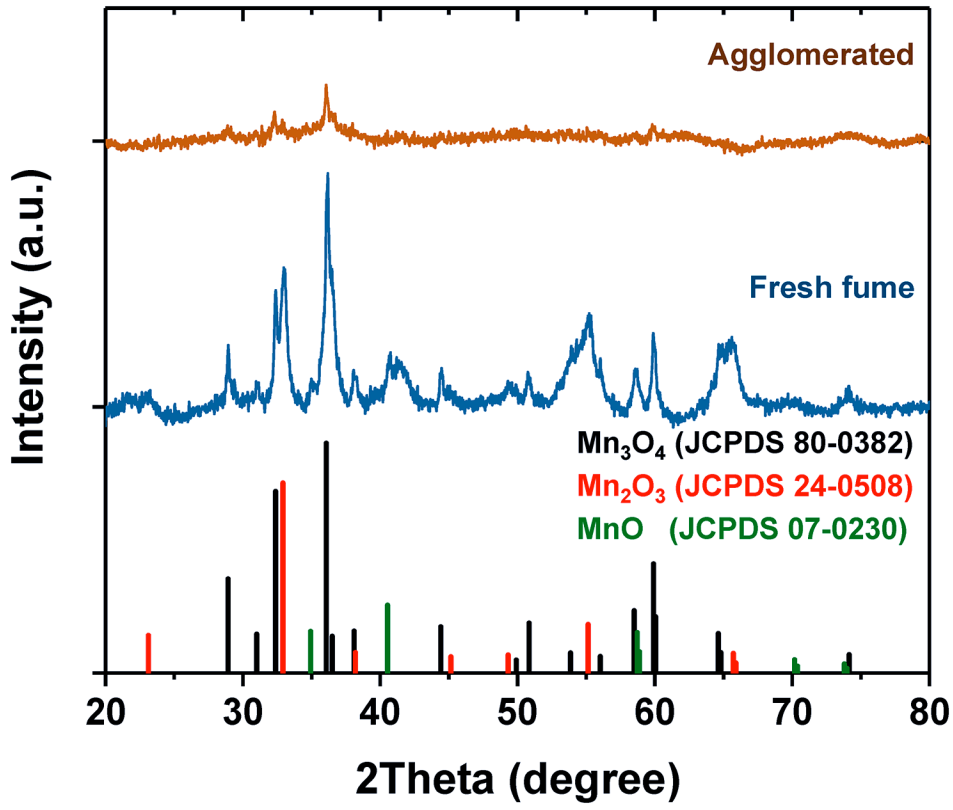

Figure 4.

X-ray diffraction patterns of fresh fume and agglomerated Mn nanoparticles compared with reference patterns of different Mn oxides available from Joint Committee on Powder Diffraction Standards card.

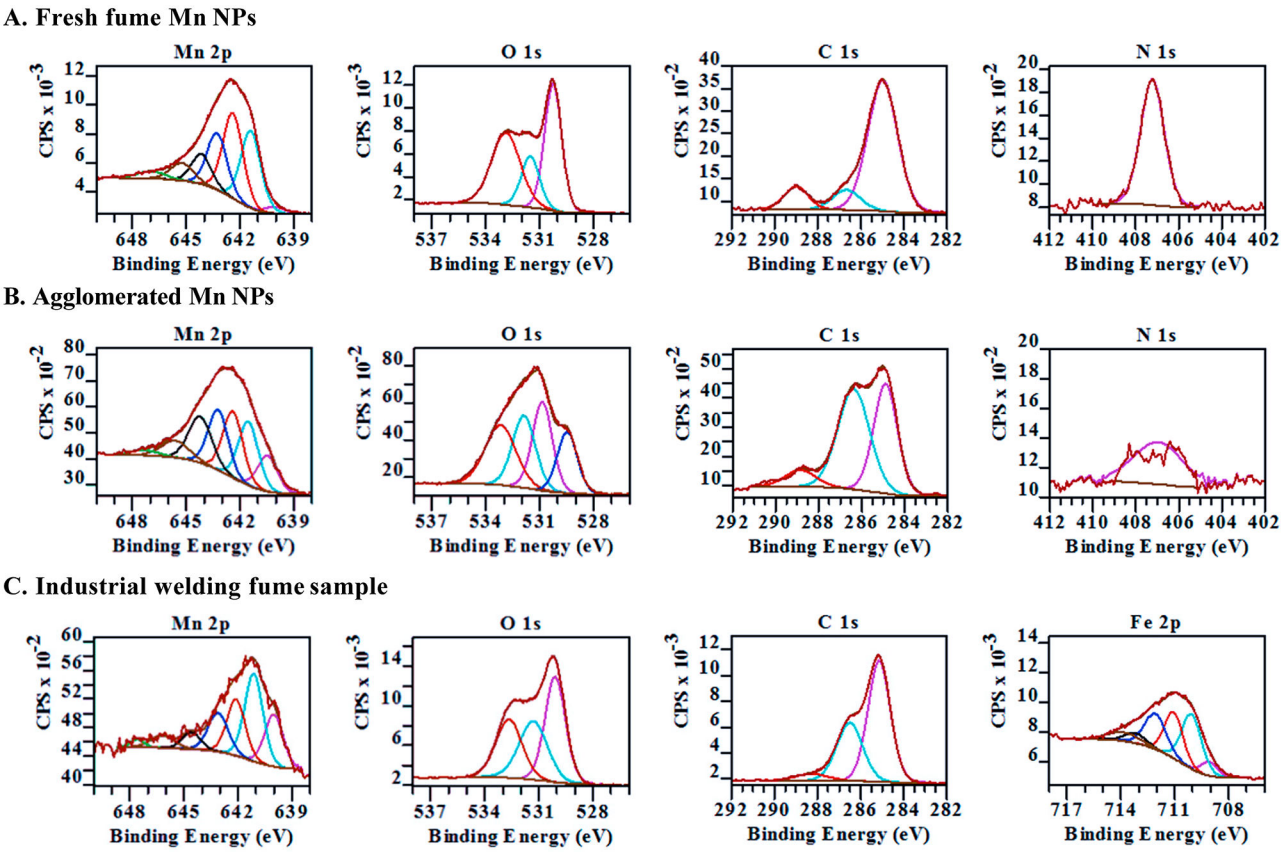

Figure 5.

High resolution XPS spectra of Mn(2p), O(1s), C(1s) and N(1s) regions for fresh fume Mn nanoparticles (A) and agglomerated Mn nanoparticles (B). High resolution XPS spectra of Mn(2p), O(1s), C(1s) and Fe(2p) regions of industrial welding sample (C).

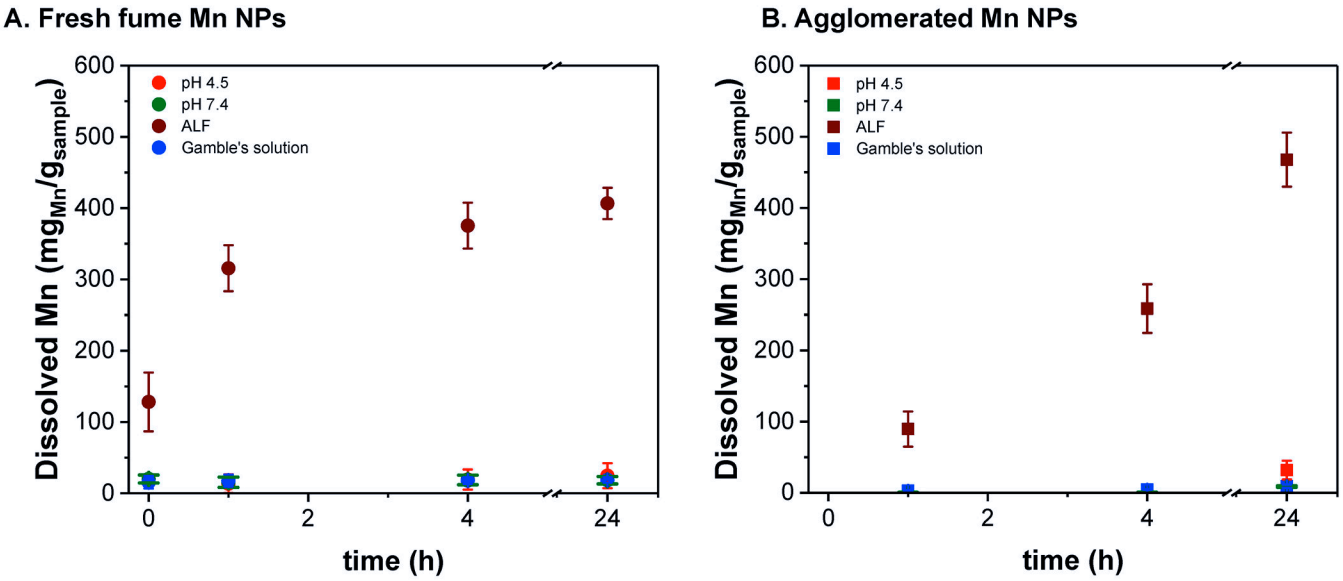

Figure 6.

Dissolution of Mn nanoparticles in simulated lung fluids, Gamble's (blue) and ALF (brown), and in pH 4.5 (red) and pH 7.4 (green) buffers.

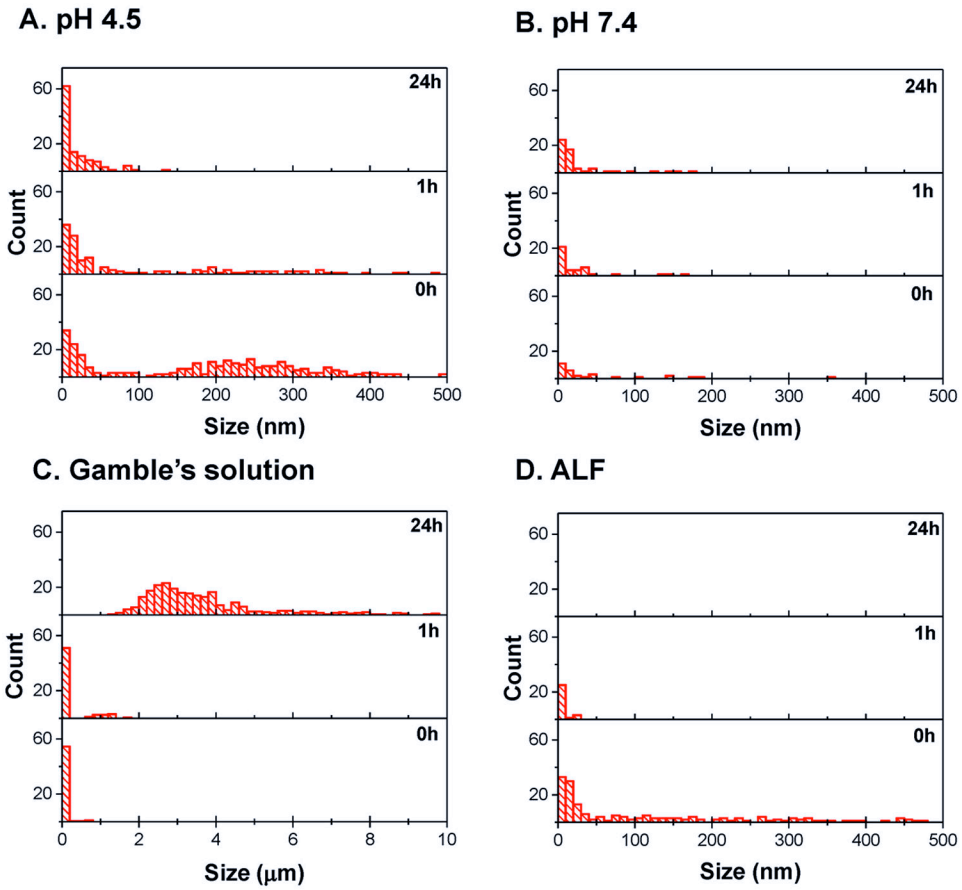

Figure 7.

DLS size analysis of fresh fume Mn nanoparticles after they were exposed to solutions with pH 4.5 (A) and pH 7.4 (B) and simulated lung fluids, Gamble's (C) and ALF (D) for 0, 1 and 24h.

Table 1.

Parameters used to generate Mn nanoparticles and associated size distributions.

Particle type	Spark current, mA	Mean diameter ± SD, nm	Total number concentration ± SD, x10^5 particle/cm^3
Fresh fume	0.5	25 ± 2	7.4 ± 0.3
	1.0	33 ± 1	10.0 ± 0.4
	2.0	41 ± 0	10.0 ± 0.0
Agglomerated nanoparticles	1.0	169 ± 5	4.2 ± 0.2
	2.5	165 ± 2	6.7 ± 0.1
	3.0	145 ± 4	6.8 ± 0.9

Table 2.

Parameters of the fitted components of XPS regions for fresh fume Mn, agglomerated Mn and welding fume samples.

		Fresh Fume Mn		Agglomerated Mn		Welding fume	
XPS region	**Peak**	**Binding Energy (FWHM), eV**	**Conc., %**	**Binding Energy (FWHM), eV**	**Conc., %**	**Binding Energy (FWHM), eV**	**Conc., %**
Mn 2p	Mn^{2+}	640.1 (1.3)	1.0	640.5 (1.3)	11.5	640.0 (1.2)	19.5
	Mn^{3+}, Mn^{2+}	641.4 (1.3)	65.9	641.5 (1.3)	20.6	641.1 (1.2)	30.9
	Mn^{3+}, Mn^{2+}	642.4 (1.3)	13.9	642.4 (1.3)	21.4	641.9 (1.2)	21.4
	Mn^{3+}, Mn^{2+}	643.3 (1.3)	9.3	643.2 (1.3)	19.4	642.9 (1.3)	19.5
	shake up	644.1 (1.3)	4.9	644.2 (1.5)	17.3	644.4 (1.2)	7.1
	shake up	645.2 (1.5)	3.3	645.6 (1.8)	7.6	646.0 (1.5)	1.2
	shake up	646.9 (1.8)	1.7	647.3 (1.8)	2.3	647.5 (1.1)	0.5
O 1s	O sorbed	--	--	529.5 (1.3)	18.9	--	--
	O^{2-}	530.3 (1.1)	41.9	530.9 (1.3)	27.3	530.1 (1.3)	40.7
	OH^{-}, CO_3^{2-}	531.5 (1.2)	18.1	531.9 (1.5)	25.6	531.3 (1.8)	31.0
	H_2O sorbed	532.9 (1.9)	40.1	533.2 (2.0)	28.3	532.7 (1.7)	28.4
C 1s	C-C	285.0 (1.6)	77.6	284.9 (1.3)	41.6	285.1 (1.2)	61.1
	C=O	286.7 (1.5)	11.3	286.4 (1.7)	50.3	286.5 (1.4)	33.8
	O-C=O	289.0 (1.3)	11.2	288.8 (1.7)	8.1	288.3 (1.8)	5.1
N 1s	NO_3^{-}	407.2 (1.3)	100.0	407.0 (2.7)	100.0	--	--
Fe 2p	pre-peak	--	--	--	--	709.1 (1.1)	6.7
	Fe^{3+} (α-FeOOH)	--	--	--	--	710.1 (1.3)	31.9
	Fe^{3+} (α-FeOOH)	--	--	--	--	711.1 (1.2)	25.0
	Fe^{3+} (α-FeOOH)	--	--	--	--	712.1 (1.4)	22.3
	Fe^{3+} (α-FeOOH)	--	--	--	--	713.2 (1.4)	6.1
	surface peak	--	--	--	--	713.9 (2.0)	8.0